# Colossal density driven resistance response in Mott-like $MnS_2$

Dylan Durkee,[1] Nathan Dasenbrock-Gammon,[2] G. Alexander Smith,[3] Elliot Snider,[4] Dean Smith,[1] Christian Childs,[1] Simon A. J. Kimber,[5] Keith V. Lawler,[3,*] Ranga P. Dias,[2,4,†] and Ashkan Salamat[1,‡]

[1] *Department of Physics & Astronomy, University of Nevada Las Vegas, Las Vegas, Nevada 89154, USA*
[2] *Department of Physics & Astronomy, University of Rochester, Rochester, New York 14627, USA*
[3] *Department of Chemistry & Biochemistry, University of Nevada Las Vegas, Las Vegas, Nevada 89154, USA*
[4] *Department of Mechanical Engineering, University of Rochester, Rochester, New York 14627, USA*
[5] *Université Bourgogne-Franche Comté, Université de Bourgogne, ICB-Laboratoire Interdisciplinaire Carnot de Bourgogne, Bâtiment Sciences Mirande, 9 Avenue Alain Savary, B-P. 47870, 21078 Dijon Cedex, France*

(Dated: July 26, 2021)

A reversible density driven insulator to metal to insulator transition in high-spin $MnS_2$ is experimentally observed, leading with a colossal electrical resistance drop of $10^8$ Ohms by 12 GPa. DFT simulations reveal the metallization to be unexpectedly driven by previously unoccupied $S_2^{2-}$ $\sigma^*_{3p}$ antibonding states crossing the Fermi level. This is a unique variant of the charge transfer insulator to metal transition for anions with an unsaturated valence. By 36 GPa the emergence of the low-spin insulating arsenopyrite ($P2_1/c$) is confirmed, and the bulk metallicity is broken with the system returning to an insulative electronic state.

Mott and charge-transfer insulators are materials where strong electron correlation localize partially filled levels, usually *d* or *f*, that would be itinerant according to band theory.[1–3] Such systems are highly sensitive, and hence tuneable, with pressure and temperature perturbations, often revealing superconducting states, spin electronics, and the ability to overcome the energetic gap and undergo insulator to metallic transitions.[4–6] Transition metal chalcogenides (TMC) present a large and diverse family of compounds that often exhibit these complex responses under density changes, undergoing transformations to dramatically different electronic and magnetic states.[7–11] The observation of colossal electroresistance under low voltage in TMCs along with rapid, reversible, phase changes between crystalline and disordered states have led to Mott memory devices and the possibility of using pressure to tune between states is an important direction for the next-generation data storage.[12] Similar response dynamics have recently been demonstrated under high pressure conditions in amorphous metallic alloys.[13]

Within the Mn chalcogenides, materials like $MnTe_2$, MnS, MnSe, $MnPS_2$, and $MnS_2$ all undergo exceptionally large volume collapse transitions which influence the electronic band structure.[14–16]. Such responses are in part a consequence of these materials being very soft, with bulk moduli of the order of 65 GPa. In the similarly soft pnictide materials, high pressure conditions cause significant changes to structural ground state, resulting from a degree of deviatoric stress present in the sample environment. For example, in $CaFe_2As_2$, superconductivity is seen in non-hydrostatic experiments, [17] but is absent in hydrostatic conditions.[18] Diffraction experiments performed under varying conditions show that this is a result of phase co-existence induced by non-hydrostatic strain.[19] Pressure-induced metallization (PIM) driven by deviatoric stress, in TMC compounds such as $MoS_2$ and $ReS_2$ show great promise for topological materials.[20, 21] Such PIM transitions also arise in other sulfide compounds, i.e $CS_2$ and OCS.[22, 23] Most notably, the recent confirmation of room temperature superconductivity, under pressure, in a carbonaceous sulfur hydride system highlights the dominant role sulfur seems to play in permitting the tailoring of exotic electronic transitions under extreme conditions.[24]

$MnS_2$ is a TMC insulator with a high-spin ($S_{Mn} = \frac{5}{2}$) pyrite phase ($Pa\bar{3}$, p-$MnS_2$) and a low-spin, ($S_{Mn} = \frac{1}{2}$) high-pressure arsenopyrite ($P2_1/c$, a-$MnS_2$) phase.[15, 25] This crystal-field driven phase transition leads to the largest reported volume collapse in any system of $\sim$22%.[15] Despite both phases of $MnS_2$ exhibiting Mott-like electronic structures,[15, 26] an insulator to metal transition has not been directly observed for either. Here we report pressure induced metallization of p-$MnS_2$ by 12 GPa, following a colossal drop in electrical resistance of $\sim$6.7 kOhms/GPa. Further compression to 36 GPa, at 300 K, reveals a spin transition into the dense arsenopyrite phase, as confirmed by in-situ synchrotron x-ray diffraction, revealing a giant volume collapse as observed at lower pressures through thermal annealing. This high density phase is non-metallic and reveals that the spin transition promotes electron localization effects that break the metallicity. All transitions are fully reversible to ambient conditions.

A total of 10 high pressure experiments were conducted on $MnS_2$ (natural specimen) in home-designed diamond anvil cells (DACs) using 300 micron culet diamonds, up to a maximum pressure of 70 GPa. Four-probe electrical resistance measurements were carried out at room and low temperature conditions. Raman spectroscopy was conducted under non-hydrostatic and quasi-hydrostatic conditions, using NaCl and He as pressure transmitting media, respectively. Synchrotron X-ray diffraction (XRD) measurements were conducted under non-

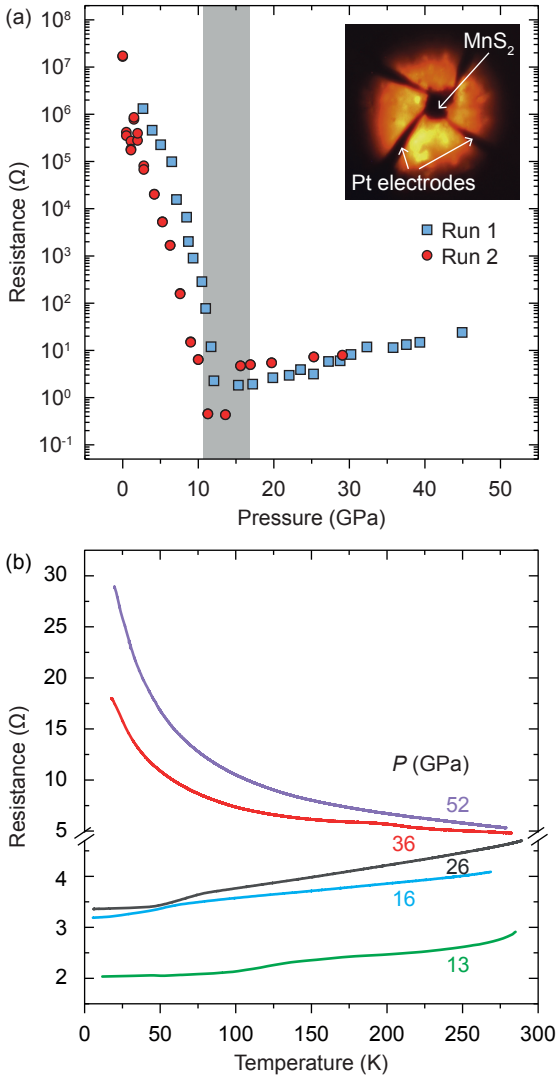


FIG. 1. (a) Electrical resistance measured across $MnS_2$ on compression to 52 GPa at room temperature in two independent runs. Note the greater than seven-order magnitude drop in resistance measured across the six different electrode pair-combinations. (inset) Microscope image of the sample loading showing the position of the leads in the sample chamber. (b) 5 independent low temperature runs at fixed pressure.

hydrostatic conditions at Sector 16, ID-B, HPCAT at the Advanced Photon Source ($\lambda = 0.4066$ Å). Samples were annealed at high pressure using an in-house $CO_2$ laser, and measured post-heating using all three experimental techniques. Density functional theory (DFT) simulations were done with VASP using the PBEsol+U [27, 28] ($U_{eff}$=3.9 eV)[29, 30] functional. Further details are in the supplemental materials.

The effect of pressure on $MnS_2$ is incredibly pronounced. Our high pressure four-probe electrical resistance measurements reveal a seven order drop in resistance within the $Pa\bar{3}$ phase (Figure 1a). By 12 GPa the system enters a metallic state as confirmed by the temperature-dependent electrical resistance, as resistance continues to decrease with a lowering in temperature (Figure 1b). At room temperature, compression above 12 GPa leads to a loss of the Raman signal of $MnS_2$ (Figure 2b). The loss of Raman signal under high pressure often is attributed to two distinct transitions; pressure induced amorphization (PIA) or disordering, and pressure induced metallization. Our XRD study reveals crystallinity throughout the full compression range, up to 52 GPa (Figure 2 bottom). As amorphization is not observed, a pressure-induced insulator to metal transition can explain the loss of Raman features as the transition to a metallic state leads to a more isotropic Fermi surface and decreases inelastic electronic scattering, leading to a very weak and smeared Raman signal.

Our DFT modelling of high-spin p-$MnS_2$ under compression confirms antiferromagnetic type-III (AFM-III) ordering for the spins of the fcc Mn sublattice.[15] The magnetic unit cell of AFM-III p-$MnS_2$ is a doubled structural unit cell in the direction parallel to the spin dipoles.[31, 32] There is increased crystal field splitting between the Mn $t_{2g}$ and $e_g$ occupied states with pressure as seen in Figure 3a-c. It is important to note that there is a consistent higher pressure difference of ∼20 GPa from our DFT work compared to our experimental results. This is a consequence of the calculations sampling a perfect crystal under hydrostatic strain at 0 K, while in contrast the experiment is conducted under non-hydrostatic conditions which provides access to lower thermodynamic barriers via non-equilibrium pathways. The crystal field splitting with pressure drives the top states of the valence band to separate from the rest of the valence band. The isolated valence band is composed of 2 spin bands per Mn, primarily representing the two half occupied $e_g$ states per Mn. The Mn $e_g$ character of those bands increases with pressure, but they still exhibit some S $p$ character at the highest pressures evaluated.

Band structure calculations reveal the onset of metallization begins when the conduction band takes on a small partial occupancy in the vicinity of the Γ-point despite a persistent 0.185 eV direct band gap at Γ (∼30 GPa). The dispersion of the valence states also increases with pressure while the separation between the valence and conduction bands decreases, indicating that the measured drop in resistance is due to a Mott-like insulator to metal transition. The gap closes entirely by 35 GPa, and Figure 3c shows the merged valence and conduction bands at 40 GPa. There is a weak (light-blue), directional sharing of charge density at 40 GPa between the Mn and S atoms that is not commensurate with an overlap of diffuse ionic charge densities (Figure 3g).

The mechanism for metallization involves the conduction band minimum (CBM) migrating below the Fermi level near the Γ point and switching identities with the valence band maximum (VBM), making the VBM composed of $S_2^{2-}$ $\sigma^*_{3p}$ states and not Mn $d$ states there. Away

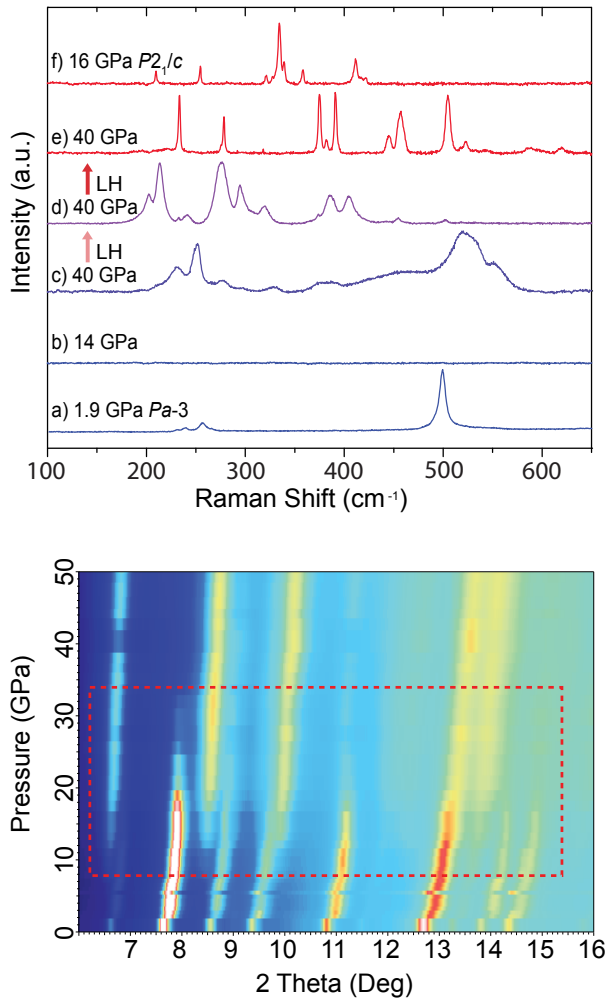


FIG. 2. Top: Raman spectra of $MnS_S$ under different conditions showing: a) the back-transformation to the ambient $Pa\bar{3}$ pyrite phase on decompression from 52 GPa; b) disappearance of the signal by 14 GPa under non-hydrostatic compression; c) emergence of a new signal after non-hydrostatic compression to 52 GPa followed by decompression to 40 GPa; d) mixed phases after $CO_2$ laser heating the sample from (c) at 40 GPa with low laser power; e) concentration of $P2_1/c$ after further $CO_2$ laser heating; and f) $P2_1/c$ signal after laser heating a hydrostatic sample at 16 GPa for comparison. Bottom: XRD density plot of $MnS_2$ with pressure. Red dashed lines emphasize the pressure region (10-36 GPa) of mixed phases. Distinct pyrite peaks are seen below 10 GPa, as well as distinct arsenopyrite peaks above 36 GPa.

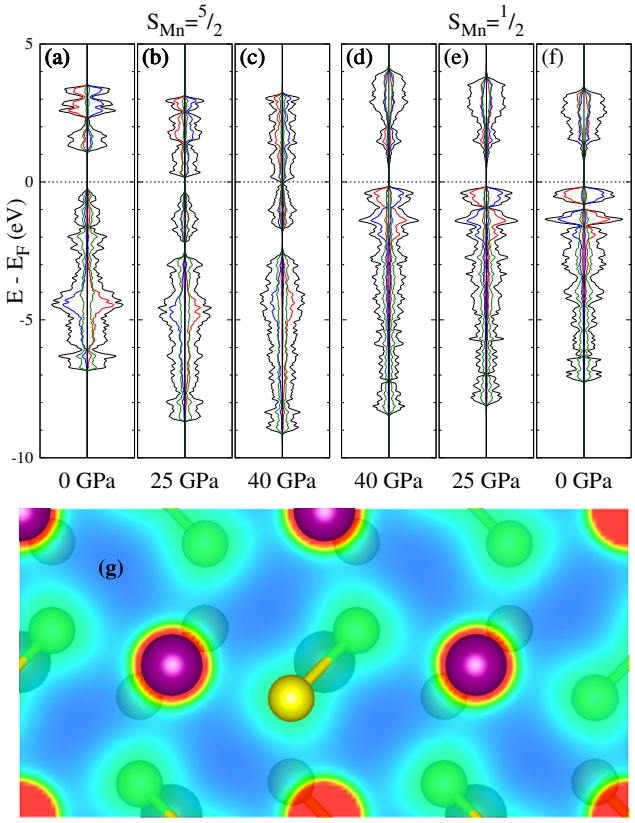


FIG. 3. Pressure dependence of the density of states (right: spin-up, left: spin-down) for high-spin (a,b,c) and low-spin (d,e,f) AFM-III pyrite(-like) $MnS_2$: total (black), spin-up Mn d (red), spin-down Mn d (blue), and summed p of an $S_2^{2-}$ (green). The partial densities are scaled by the number of equivalent ions. (g) The charge density in (010) of high-spin AFM-III pyrite-like $MnS_2$ at 40 GPa, saturation at 20% of maximum.

from Γ the CBM and VBM retain similar compositions as at lower pressures (plots in Supplemental). There is also a drop in the computed magnetic moment per Mn with increased pressure – from 4.48 $\mu_B$ at 0 GPa to 3.84 $\mu_B$ at 40 GPa. This equates to a transfer/hybridization of around half an electron per Mn into the $S_2$ states when $MnS_2$ metallizes. This is opposed to a typical charge-transfer insulator to metal transition wherein occupied ligand $p$ bands merge with unoccupied metal $d$ bands.[3] This mechanism for metallization is unique to systems with molecular ions that have unsaturated valences. The changing identity of the VBM and CBM and increased metal-to-ligand charge transfer (MLCT) with pressure could explain the evolution of the XANES spectrum of $MnS_2$ under cold compression,[30] as the pre-edge feature is most likely building in with pressure from an increased accessibility of unoccupied Mn $d$ states for electric quadrupolar Mn $1s \rightarrow 3d$ excitations.[33–36] More detailed spectroscopic calculations are needed to confirm this.

The DFT structural optimizations show symmetry lowering distortions as early as 5 GPa. This includes a slight breaking of $a$=$b$ symmetry [37] from pronounced "0 K" magneto-elastic distortions along the magnetic propagation vector [38] (table in Supplemental). Although our experimental XRD can not resolve such subtle distortions to orthorhombic $Pbc2_1$, we do observe some peak broadening. The retention of a pyrite-

like phase is similar to another Mn dichalcogenide, $MnTe_2$, where Mössbauer spectroscopy indicates that a pyrite structure is retained after pressure induced metallization.[14]

Further compression above 36 GPa reveals a nexus of electronic and structural change in the experimental measurements. Four-probe electrical measurements show an increase in resistance with increasing pressure and a lowering of temperature. This is indicative of a semi-conducting state and opposite to the electronic transition at 12 GPa; the energy-density tuning drives a metal-insulator transition. Figure 1b shows that for temperature cooling runs at 36 and 52 GPa, there is a greater increase and hence a larger electronic band gap with pressure, respectively. This transition is followed by a change in the spectroscopic response as the Raman signal returns with a new set of features. The return to a non-metallic state, with a band gap, increases the polarizablity of more delocalized surface-plasmons, which leads to the reemergence of the Raman spectra above 40 GPa with features that resemble pyrite-like optical modes (Figure 2c). Subsequent decompression after the return of the Raman signal leads to the eventual split of the main feature relating to S-S stretching mode split into three distinct features. The reemergence of Raman signal is highly dependant on deviatoric stress in the sample; in the case of quasi-hydrostatic compression in He, Raman activity is not registered up to 70 GPa.

Synchrotron x-ray diffraction reveals a transformation at 36 GPa to a-$MnS_2$, following a giant volume collapse of ~20%, as previously reported.[15] This structural transition remarkably is confirmed here at room temperature, whilst previously the high density ground-state arsenopyrite phase was reported via laser heating above 1500 K at 12 GPa.[15] This significant difference in conditions is, in part, driven by deviatoric stress from the non-hydrostatic conditions of this experiment and most likely a negative Clausius–Clapeyron slope of the phase boundary. Upon decompression the system undergoes a back transformation to the ambient pyrite structure at 5 GPa.

At 40 GPa, electrical resistance was measured in between successive laser heating intervals, resulting in a decrease in conductivity. This corresponds to the reduction in the phase coexistence, with a diminishing fraction of the pyrite-like $MnS_2$, arising from kinetic hindrance. Upon decompression, a re-emergence of the main pyrite Raman peak is observed; the $A_g$ stretching feature at 480 $cm^{-1}$ by ambient pressure. There is also a feature present in all Raman spectra taken during transport measurements, both on compression and decompression; this feature appears around 700-800 $cm^{-1}$. The origin of this feature is not identified.

Like with other Mn compounds, the transition to the low-spin phase of $MnS_2$ under pressure is accompanied by a giant volume collapse.[15, 16, 39] An increased crystal field splitting from the initial weak field of the octahedrally coordinated $S_2^{2-}$ ions eventually favors a low-spin configuration occupying just the Mn $t_{2g}$ orbitals over half-occupancy of all 5 $Mn^{2+}$ $d$-orbitals, thus triggering the transformation into the arsenopyrite phase.[15, 26] At the pressures previously examined (0-20 GPa), high temperature is necessary to drive high-spin pyrite $MnS_2$ into the ground, low-spin arsenopyrite phase. Prior to heating there is a disordered intermediate phase with the same oxidation state as both the pyrite and arsenopyrite phases and a XANES spectrum similar to the laser annealed arsenopyrite phase.[30] The formation of the low-spin arsenopyrite phase entails the formation of Mn–Mn bonds remarked by alternating short-long Mn–Mn distances along [$\bar{1}$01]. These Mn–Mn bonds do not result in metallization of the system unlike the two-dimensional honeycomb antiferromagnets $MnPS_3$ and $MnPSe_3$, where Mn–Mn metallic bonds formed under high pressure result in a semi-metal.[40]

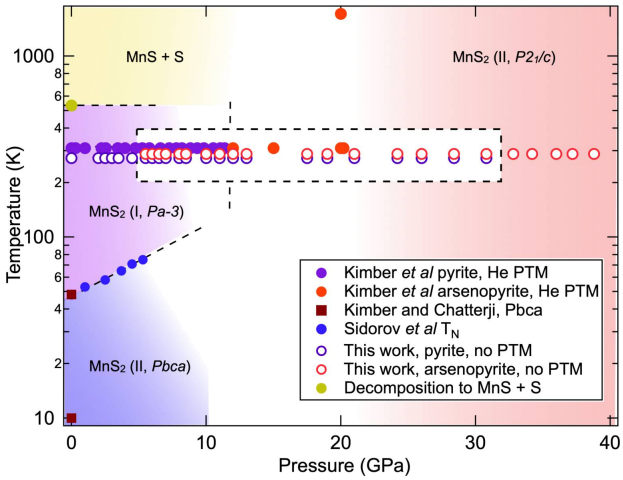


FIG. 4. T-P phase diagram of $MnS_2$. Until around 12 GPa, the pyrite phase is sensitive to decomposition to MnS + S through additional heat. Purple data points track pyrite $Pa\bar{3}$ $MnS_2$ to around 12 GPa, where $P2_1/c$ is accessible via laser heating (shown by red data points).[15] Blue data points track the Néel temperature as a function of pressure,[41] separating the AFM *Pbca* phase [37] from the paramagnetic pyrite phase.

DFT confirms that by 20 GPa of hydrostatic pressure antiferromagnetic a-$MnS_2$ is the true ground state structure. This was checked by both homologue optimizations and a non-spin polarized crystal structure search at 50 GPa. The proposed marcasite (*Pnnm*, m-$MnS_2$) structure was also evaluated in detail in a non-spin polarized, ferromagnetic (FM), and AFM (magnetic polarization following [001]) form.[42, 43] The 0, 11, 20, and 50 GPa optimized structures for m-$MnS_2$ are nearly identical to those of a-$MnS_2$ with a consistent preferred energy ordering of AFM > FM > non-spin polarized. In each instance, the magnetic solutions for a-$MnS_2$ and m-$MnS_2$ adopt a low-spin state with a magnetic moment

around 1 $\mu_B$; the persevering moments indicate that even 50 GPa is not enough to form 1-D metal bonded chains.

Continuing to compress high-spin AFM-III pyrite-like $MnS_2$ would potentially increase the MLCT enough to trigger the $Mn^{2+} + S_2^{2-} \rightarrow Mn^{4+} + 2S^{2-}$ reaction, however the metallic, high-spin phase is meta-stable. Beyond 40 GPa the DFT optimizations collapse into a low-spin ($S_{Mn} = \frac{1}{2}$) AFM-III, orthorhombically distorted pyrite $MnS_2$ phase that is non-metallic (Figure 3d-f). As in a-$MnS_2$, the transition into low-spin AFM-III pyrite-like $MnS_2$ is accompanied by a large volume collapse. Low-spin AFM-III pyrite-like $MnS_2$ is 23.6% smaller than the high-spin phase at 0 GPa, and this margin narrows to 11.8% at 40 GPa. The low-spin phase becomes enthalpically more favorable than the high-spin phase at 25 GPa (ignoring vibrational free energy contributions), meaning that the observed metallic phase is meta-stable supported by a combination of kinetic hindrance and deviatoric stresses.

In summary, an insulator to metal transition is measured in $MnS_2$, with a colossal seven order drop in resistance over a modest pressure range of 12 GPa. DFT simulations indicate the metallization occurs via unoccupied $S_2^{2-}$ $\sigma^*_{3p}$ antibonding states crossing the Fermi level resulting in ~0.5 electrons/Mn of metal-to-ligand charge transfer. This variation of a charge transfer insulator-to-metal transition is unique to anions with unsaturated valences. Metallic $MnS_2$ transforms into the arsenopyrite structure at 36 GPa, and that transformation is accompanied by a giant volume collapse arising from a high-to-low spin transformation of the $Mn^{2+}$ ions. Transformation into the arsenopyrite phase returns $MnS_2$ to an insulator as is confirmed by resistance measurements and DFT. These results are not only pertinent to understanding manganese dichalcogenides, but also in establishing a better understanding of the electron correlation effects in related materials. In particular, this includes systems with molecular anions and across the group 7 elements where electron correlation effects produce very different structures for materials of similar composition.[44]

This paper is dedicated to Tapan Chatterji, without whom this work would have been impossible. This material is based upon work supported by the National Science Foundation Division of Materials Research under Grant No. 1904694. ND-G, ES, and RPD were supported by NSF, Grant No. DMR-1809649; DOE Stockpile Stewardship Academic Alliance Program, Grant No. DE-NA0003898; and U.S. Department of Energy, Office of Science, Fusion Energy Sciences under Award Number DE-SC0020340. SAJK était soutenu par le programme « Investissements d'Avenir », projet ISITE-BFC (contrat ANR-15-IDEX-0003). Computational resources provided by the UNLV National Supercomputing Institute.

* keith.lawler@unlv.edu
† rdias@rochester.edu
‡ salamat@physics.unlv.edu

[1] N. F. Mott, Rev. Mod. Phys. **40**, 677 (1968).
[2] J. Zaanen, G. A. Sawatzky, and J. W. Allen, Phys. Rev. Lett. **55**, 418 (1985).
[3] M. Imada, A. Fujimori, and Y. Tokura, Rev. Mod. Phys. **70**, 1039 (1998).
[4] M. P. Pasternak, G. K. Rozenberg, G. Y. Machavariani, O. Naaman, R. D. Taylor, and R. Jeanloz, Phys. Rev. Lett. **82**, 4663 (1999).
[5] A. G. Gavriliuk, V. V. Struzhkin, I. S. Lyubutin, S. G. Ovchinnikov, M. Y. Hu, and P. Chow, Phys. Rev. B **77**, 155112 (2008).
[6] A. G. Gavriliuk, I. A. Trojan, and V. V. Struzhkin, Phys. Rev. Lett. **109**, 086402 (2012).
[7] H. Luo, R. G. Greene, K. Ghandehari, T. Li, and A. L. Ruoff, Phys. Rev. B **50**, 16232 (1994).
[8] Z. Du, S. Yang, S. Li, J. Lou, S. Zhang, S. Wang, B. Li, Y. Gong, L. Song, X. Zou, and P. M. Ajayan, Nature **577**, 492– (2020).
[9] T. Bither, C. Prewitt, J. Gillson, P. Bierstedt, R. Flippen, and H. Young, Solid State Communications **4**, 533 (1966).
[10] H. Wang, H. Yuan, S. Sae Hong, Y. Li, and Y. Cui, Chem. Soc. Rev. **44**, 2664 (2015).
[11] X.-C. Pan, X. Chen, H. Liu, Y. Feng, Z. Wei, Y. Zhou, Z. Chi, L. Pi, F. Yen, F. Song, X. Wan, Z. Yang, B. Wang, G. Wang, and Y. Zhang, Nature Communications **6**, 7805 (2015).
[12] L. Zhu, J. Zhou, Z. Guo, and Z. Sun, Journal of Materiomics **1**, 285 (2015).
[13] M. Xu, Y. Q. Cheng, L. Wang, H. W. Sheng, Y. Meng, W. G. Yang, X. D. Han, and E. Ma, Proceedings of the National Academy of Sciences **109**, E1055 (2012).
[14] P. Vulliet, J. P. Sanchez, D. Braithwaite, M. Amanowicz, and B. Malaman, Physical Review B **63**, 184403 (2001).
[15] S. A. J. Kimber, A. Salamat, S. R. Evans, H. O. Jeschke, K. Muthukumar, M. Tomi, F. Salvat-Pujol, R. Valenti, M. V. Kaisheva, I. Zizak, and T. Chatterji, Proceedings of the National Academy of Sciences **111**, 5106 (2014).
[16] Y. Wang, L. Bai, T. Wen, L. Yang, H. Gou, Y. Xiao, P. Chow, M. Pravica, W. Yang, and Y. Zhao, Angewandte Chemie International Edition **55**, 10350 (2016).
[17] M. S. Torikachvili, S. L. Bud'ko, N. Ni, and P. C. Canfield, Phys. Rev. Lett. **101**, 057006 (2008).
[18] W. Yu, A. A. Aczel, T. J. Williams, S. L. Bud'ko, N. Ni, P. C. Canfield, and G. M. Luke, Phys. Rev. B **79**, 020511 (2009).
[19] A. I. Goldman, A. Kreyssig, K. Prokeš, D. K. Pratt, D. N. Argyriou, J. W. Lynn, S. Nandi, S. A. J. Kimber, Y. Chen, Y. B. Lee, G. Samolyuk, J. B. Leão, S. J. Poulton, S. L. Bud'ko, N. Ni, P. C. Canfield, B. N. Harmon, and R. J. McQueeney, Phys. Rev. B **79**, 024513 (2009).
[20] A. P. Nayak, S. Bhattacharyya, J. Zhu, J. Liu, X. Wu, T. Pandey, C. Jin, A. K. Singh, D. Akinwande, and J.-F. Lin, Nature Communications **5**, 3731 (2014).
[21] D. Zhou, Y. Zhou, C. Pu, X. Chen, P. Lu, X. Wang, C. An, Y. Zhou, F. Miao, C.-H. Ho, J. Sun, Z. Yang, and D. Xing, npj Quantum Materials **2**, 19 (2017).

[22] R. P. Dias, C.-S. Yoo, M. Kim, and J. S. Tse, Physical Review B **84**, 144104 (2011).

[23] M. Kim, R. Dias, Y. Ohishi, T. Matsuoka, J.-Y. Chen, and C.-S. Yoo, Scientific Reports **6** (2016), 10.1038/srep31594.

[24] E. Snider, N. Dasenbrock-Gammon, R. McBride, M. Debessai, H. Vindana, K. Vencatasamy, K. V. Lawler, A. Salamat, and R. P. Dias, Nature **586**, 373 (2020).

[25] G. Brostigen and A. Kjekshus, Acta Chemica Scandinavica **24**, 2993 (1970).

[26] A. Rohrbach, J. Hafner, and G. Kresse, Journal of Physics: Condensed Matter **15**, 979 (2003).

[27] G. I. Csonka, J. P. Perdew, A. Ruzsinszky, P. H. T. Philipsen, S. Lebègue, J. Paier, O. A. Vydrov, and J. G. Ángyán, Phys. Rev. B **79**, 155107 (2009).

[28] S. L. Dudarev, G. A. Botton, S. Y. Savrasov, C. J. Humphreys, and A. P. Sutton, Phys. Rev. B **57**, 1505 (1998).

[29] L. Wang, T. Maxisch, and G. Ceder, Phys. Rev. B **73**, 195107 (2006).

[30] D. Durkee, D. Smith, R. Torchio, S. Petitgirard, R. Briggs, I. Kantor, S. R. Evans, T. Chatterji, T. Irifune, S. Pascarelli, K. V. Lawler, A. Salamat, and S. A. Kimber, Journal of Solid State Chemistry **269**, 540 (2019).

[31] L. M. Corliss, N. Elliott, and J. M. Hastings, Journal of Applied Physics **29**, 391 (1958).

[32] J. M. Hastings, N. Elliott, and L. M. Corliss, Phys. Rev. **115**, 13 (1959).

[33] A. V. Soldatov, T. S. Ivanchenko, A. P. Kovtun, S. Della Longa, and A. Bianconi, Phys. Rev. B **52**, 11757 (1995).

[34] F. m. c. Farges, Phys. Rev. B **71**, 155109 (2005).

[35] K.-W. Nam, M. G. Kim, and K.-B. Kim, The Journal of Physical Chemistry C **111**, 749 (2007).

[36] T. Yamamoto, X-Ray Spectrometry **37**, 572 (2008).

[37] S. A. J. Kimber and T. Chatterji, Journal of Physics: Condensed Matter **27**, 226003 (2015).

[38] T. Chatterji, in *Neutron Scattering from Magnetic Materials*, edited by T. Chatterji (Elsevier Science, Amsterdam, 2006) pp. 25 – 91.

[39] H. Fjellvåg, A. Kjekshus, T. Chattopadhyay, H. Hochheimer, W. Hönle, and H. V. Schnering, Physics Letters A **112**, 411 (1985).

[40] Y. Wang, J. Ying, Z. Zhou, J. Sun, T. Wen, Y. Zhou, N. Li, Q. Zhang, F. Han, Y. Xiao, P. Chow, W. Yang, V. V. Struzhkin, Y. Zhao, and H. K. Mao, Nature Communications **9**, 1914 (2018).

[41] V. A. Sidorov, J. Guo, L. Sun, and V. V. Brazhkin, JETP Letters **107**, 311 (2018).

[42] T. Chattopadhyay and H. von Schnering, Journal of Physics and Chemistry of Solids **46**, 113 (1985).

[43] T. Chattopadhyay, H. von Schnering, and W. Grosshans, Physica B+C **139-140**, 305 (1986).

[44] K. V. Lawler, B. C. Childs, D. S. Mast, K. R. Czerwinski, A. P. Sattelberger, F. Poineau, and P. M. Forster, Inorganic Chemistry **56**, 2448 (2017).